Automatic real-time guidance of laser machining with inline coherent imaging

Paul J. L. Webster,[a] Logan G. Wright, Kevin D. Mortimer, Ben Y. Leung,
Joe X. Z. Yu, and James M. Fraser
*Department of Physics, Engineering Physics and Astronomy, Queen's University, Kingston,
Ontario K7L 3N6, Canada*

Optical coherence imaging can measure hole depth in real-time (>20 kHz) during laser drilling without being blinded by intense machining light or incoherent plasma emissions. Rapid measurement of etch rate and stochastic melt relaxation makes these images useful for process development and quality control in a variety of materials including metals, semiconductors, and dielectrics. The ability to image through the ablation crater in materials transparent to imaging light allows the guidance of blind hole cutting even with limited *a priori* knowledge of the sample. Significant improvement in hole depth accuracy with the application of manual feedback from this imaging has been previously demonstrated [P. J. L. Webster *et al.*, Opt. Lett. **35**, 646 (2010)]. However, the large quantity of raw data and computing overhead are obstacles for the application of coherent imaging as a truly automatic feedback mechanism. Additionally, the high performance components of coherent imaging systems designed for their traditional application in biological imaging are costly and may be unnecessary for materials processing. In this work, we present a coherent imaging system design that costs less than a fifth of comparable commercial products. We also demonstrate streamlined image processing suited for automated feedback that increases processing speed by two orders of magnitude. © *2011 Laser Institute of America.*

Key words: inline coherent imaging, process monitoring, process control

I. INTRODUCTION

Laser processing has the advantage that a single laser can be used to clean, weld, and/or machine different materials without mechanical adjustment or changing chemical treatments. Although laser ablation of heterogeneous or multilayered samples has been accomplished (e.g., Ref. 1), these processes require tremendous amounts of development and rely on uniform sample characteristics or models with limited applicability and varied success.[2] Laser welding and cleaning, too, typically require extensive multiparameter optimization.[3,4] This problem of achieving a specific set of processing objectives (feature aspect ratio,[2] heat affected zone, etc.) within the available parameter space (encompassing feed rate, pulse energy, pulse duration, wavelength, assist gas, spot size, and focal position) is compounded by the characteristics of the material (ablation threshold and polymer molecular weight[5]). Accordingly, industrial laser process development requires significant time and financial investment, and may demand fine tolerance feedstock to ensure reliability.

These challenges and costs may be circumvented using real-time observation and adaptive control, particularly in materials with heterogeneous or dynamic geometry, or unstable absorption characteristics. Depth sensing in particular has great potential for controlling processes such as drilling printed circuit board vias or defect correction with little to no precharacterization of the sample.[6] Despite a large body of literature of surface measurement techniques,[7] only optical techniques can avoid being destroyed by the machining process while also meeting requirements for speed and compatibility with high aspect ratio holes. However, the right optical instrument must still overcome many challenges inherent to imaging intense light-matter interactions such as large variations in backscatter due to rapidly changing geometry and physical state, simultaneous reflections from multiple depths, blinding scatter of the intense machining beam, and strong broadband optical emissions from plasma. Therefore, in addition to resolution on the order of ~ 10 μm and rapid high duty cycle acquisition, an effective system must also have high dynamic range and high sensitivity, and be resistant to blinding by plasma and machining light. Based on a survey of processing lasers and applications, real-time acquisition on the order of the pulse repetition rate of commonly used lasers (tens of kilohertz or less) should allow depth sensing in most processes. A final nontechnical requirement is that an instrument would likely need to be available at a cost of $\sim\$10\,000$ in order to reach a wide range of applications.

Several groups have demonstrated optical instruments that can monitor hole depth during percussion drilling. Temnov *et al.*[8] used time-resolved Linnik interferometry to achieve nanometer spatial and femtosecond temporal resolution. However, they imaged in delayed time (not real-time) and reflections originating from side walls in high aspect ratio holes might corrupt the measurement. Dietrich *et al.*[9] used high speed photography of deformations of the bulk

caused by hole drilling near an edge. They followed hole depth over many millimeters, but this approach is geometrically restrictive (cutting must be near an edge) and indirect. Lausten *et al.*[10] measured hole depth with a nonlinear cross-correlation of light backscattered from holes during drilling, but the acquisition rate was limited to 1 kHz by the repetition rate of their femtosecond light source. Furthermore, the high speed area-scan cameras and/or ultrafast laser sources used by these groups make their systems too expensive for the majority of applications. We recently demonstrated an inline coherent imaging (ICI) system that is capable of guiding blind hole percussion drilling and sensing melt pool dynamics in holes several hundred micrometers deep.[11] This imaging technique is based on white light interferometry measured in the spectral domain and processed in a manner similar to spectral domain optical coherence tomography (SD-OCT).[12] A recent advance in complementary metal-oxide semiconductor line camera technology has allowed us to increase acquisition rates to >300 kHz and observe the temporal dynamics of the melt pool in greater detail.[13] This system provides a real-time measurement of the effect of common process parameters (e.g., assist gas) on the etch rate and relaxation of the sample. We now aim to extend the practicality of ICI and enable automatic feedback by improving two key criteria: cost and processing speed.

In rapid volumetric biological coherent imaging, obtaining high resolution and a useful signal-to-noise ratio deep in turbid media requires expensive components: a broadband light source with >50 nm bandwidth and >100 mW average power, a top performance line camera, and very fast galvanometer scanners. The demands of the present material imaging application are less intensive. Typically, machining samples are highly reflective, so biological-grade sensitivities of >100 dB are not necessary. Also, by limiting imaging to the machining axis and not acquiring over a large volume, sufficiently high temporal resolution can be achieved with an economical camera.

Computational load is the second criteria. High speed acquisition is of limited value for high duty cycle feedback control if signal processing is the true bottleneck. Standard SD-OCT processing requires numerical interpolation (usually cubic spline interpolation for best quality) from wavelength to wavenumber bases and a fast Fourier transform (FFT) of several hundred data points. These calculations are computationally intensive, requiring more expensive/complex computer hardware and/or limiting the response time of an automatic feedback loop.

In this paper, we present a step toward overcoming these limitations. First, a low cost imaging system design optimized for laser drilling/welding applications is described at component level detail with calculated key performance metrics. Second, a novel processing method based on homodyne filtering that bypasses the most complicated computations is discussed and compared to standard methods.

II. BACKGROUND

The coherent imaging technique used here borrows optical and image processing techniques from the field of spectral domain optical coherence tomography (SD-OCT).[12] OCT has been described as the optical analog of ultrasound imaging. The measurement uses a white light optical fiber interferometer to obtain the optical path length (OPL) of an object relative to a fixed reference length. In the spectral domain, the relative OPL of the sample reflection is encoded in the spacing of the spectral interference fringes in the output from the interferometer. Specifically, consider a set of p reflectors in the sample arm, each with an OPL difference from the reference length of z_i. The resulting spectral interferogram intensity is approximately

$$I(k) = A(k)\sum_{i=1}^{p}\left[\frac{I_{ref}}{2p} + \frac{I_i}{2} + \sqrt{I_{ref}I_i}\cos(2kz_i)\right]. \qquad (1)$$

$A(k)$ is the spectral envelope of the imaging light source and k is the wavenumber. The first term is known *a priori* and can be subtracted as a background signal. The second term is typically very small and can be neglected. In the third term, the weak sample reflection (I_i) has its intensity multiplied by the strong reference signal and appears as a sinusoidal interference fringe whose spacing (i.e., frequency) depends on its depth (z_i). Since each depth corresponds to a different fringe frequency, the signals are orthogonal and can be monitored independently with no moving parts. Acquisition speed and signal-to-noise are therefore limited by the detector and the intensity of the imaging light. It should be emphasized that ICI can work coaxially with the machining beam, enabling depth sensing with hole aspect ratios much higher than would be possible with triangulation methods.

To extract depth information, the spectral interferogram (measured with a spectrometer) is resampled to units of constant wavenumber by interpolation and transformed to $I(z)$ via FFT. The resulting function (known as an A-scan or A-line) is a depth-reflectivity profile of the sample (shown in logarithmic units relative to the noise floor) with each reflecting interface in the sample appearing as a point spread function (PSF) centered about its depth. The PSF full width at half maximum (FWHM) is usually referred to as the axial resolution of the system, and for Gaussian $A(k)$,

$$\delta z = \frac{2\ln 2}{\pi}\frac{\lambda^2}{\Delta\lambda}. \qquad (2)$$

Thus, a short center wavelength (λ) of the light source and broad spectrum ($\Delta\lambda$) are desired for high resolution imaging. Typical axial resolutions in biological imaging on the order $5-10$ μm are achieved with quasi Gaussian spectra of 830 ± 30 nm FWHM (ophthalmology) or 1310 ± 35 nm FWHM (scattering tissue).

One important imaging artifact arises due to the ambiguity between positive and negative OPL (z_i and $-z_i$ yield the same interferogram). Since the spectral interferogram is purely real, the depth-reflected profile has complex conjugate symmetry of about zero. Half the image is usually discarded, leaving only positive OPLs. However, if a reflecting interface is located on the negative side of the reference point, its signature wraps back into the image as an artifact. Thus, a system must be designed with an adequate depth field of
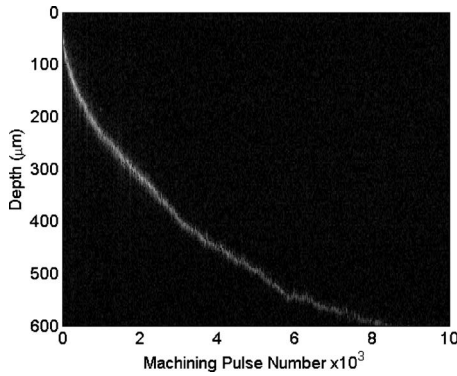
FIG. 1. Real-time M-mode image of percussion drilling in steel. 760 μJ pulses are incident onto a 20 μm e^{-2} intensity diameter spot at 30 kHz. A coaxial oxygen assist gas jet at 8.3 bars is used. Imaging rate is 300 kHz. Graph brightness corresponds to sample reflectivity in logarithmic scale. The dynamic range shown is ~60 dB.

view (FOV) and care must be taken to ensure that all reflecting interfaces are located on only side of the zero delay.

To create an image, many spectral interferograms are acquired serially by the spectrometer, processed into A-lines, and then displayed as a three dimensional data set of reflectivity versus depth versus A-line number. In biological imaging, the A-line number corresponds to the transverse position as the imaging beam is raster scanned. This produces an image of reflectivity as a function of two spatial dimensions known as a B-mode image (B=brightness). Alternatively, if the beam is static, the A-line number corresponds to time and the resulting image is called an M-mode image (M =motion). This type of image is useful for observing fast changes in the depth-reflectivity profile of the sample. For example, coaxial imaging during the percussion drilling of 304 stainless steel with a 1070 nm center wavelength, 100 ns duration fiber laser (IPG YLP-1/100/30/30-HC) gives the M-mode image in Fig. 1. The machining front (bright white curve) is seen descending ~600 μm into the bulk of the sample. The complete etch depth versus pulse number relationship is obtained from drilling a single hole and requires no postcut material processing.

With acquisition rates of even a few tens of kilohertz, M-mode images are not only able to directly measure etch rates[13,14] but also melt pool flow[11] and other dynamics of laser drilling processes.[15] Since sensing below the machining front is possible, M-mode data can also be used to guide blind hole cutting in a variety of semitransparent materials including biological tissue[16] even when the exact sample geometry is not known *a priori*.

III. SYSTEM DESIGN

We have designed a low cost (<$10 000) coherent imaging system with an imaging rate of 27 kHz that is suitable for use in industrial laser materials processing applications. A deep FOV is emphasized over very high resolution to tolerate sample variability and alignment imprecision. Furthermore, a deep FOV allows more material removal before a mechanical adjustment is necessary. It is expected that a
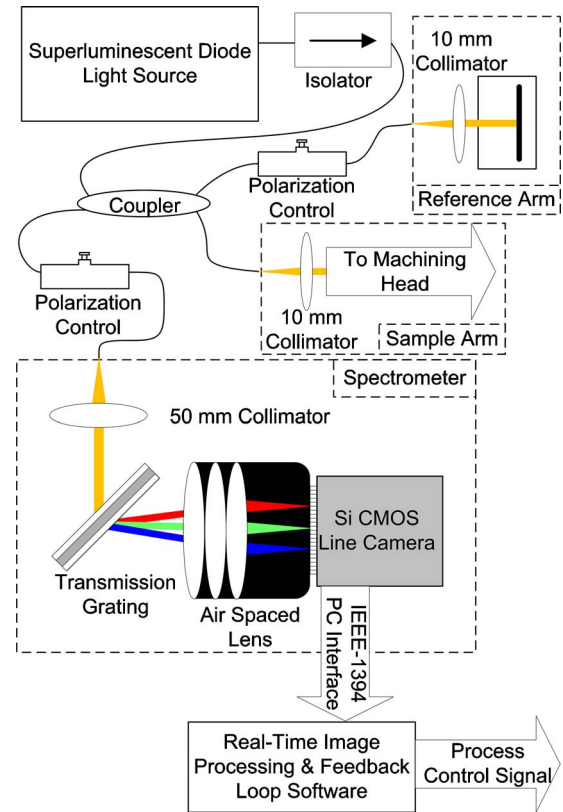

FIG. 2. Schematic diagram of the proposed imaging system and feedback mechanism.

FOV of several millimeters will exceed the useful depth of focus of most laser microprocessing systems and therefore be adequate for these applications.

The proposed system is comprised of a fiber-coupled superluminescent diode (SLD), a custom spectrometer, and a fiber optic Michelson interferometer that can be interfaced to a laser machining head (Figure 2 provides a schematic layout). Imaging light from the SLD first passes through an optical isolator, which protects the SLD from back-reflection. The light continues into an evanescent mode coupler (beam splitter) where it is split into the sample and reference arms, then coupled out of the fiber and into free space. Some light is retroreflected in both interferometer arms and the signals are recombined and interfere at the mode coupler. Polarization controllers correct for mismatches between the two interferometer arms arising from polarization effects in single mode fiber and also to optimize diffraction grating efficiency. A transmission grating is used in the spectrometer for ease of alignment. Finally, the camera measures the spectral interferogram and transmits data via IEEE-1394 to a desktop computer for processing.

Using design equations present in the SD-OCT literature for spectrometer configuration, signal strength, and noise sources[12,17–19] along with the available specifications for our components (specified below), we obtain a best-case estimate of the system's key performance figures, as summarized in Table I.

As cost is a major factor in this design, a detailed breakdown of the components is provided in Table II. Even with-

TABLE I. Calculated system performance characteristics.

Axial resolution (μm)	**12**
Depth of field (mm)	**5.9**
Maximum line rate (kHz)	**27**
Duty cycle (IEEE-1394 interface limited)	**73%**
Sensitivity (dB)[a,b] (35 μs integration)	**97**
Sensitivity (dB)[a,b] (1 μs integration)	**76**
Sensitivity (dB)[a,b] (100 ns integration)	**61**
Max. dynamic range (dB)[a]	**68**

[a]Based on noise specifications available for camera operating at low speed. Actual value is expected to be lower at full speed.
[b]Assumes sample arm optics have ~80% efficiency.

TABLE II. Imaging system components price list.

Component	Price ($)
Light source:	**2025**
• Exalos EXS8310-F411 superluminescent diode (830 ± 13 nm FWHM)	1275
• Exalos EBD5010 SLD driver	725
• Thorlabs TPS101 −5 V power supply unit	25
Mode coupler:	**255**
Thorlabs FC850–40–50-APC 2 × 2 broadband SM coupler	255
Polarization controllers:	**500**
2-General Photonics miniature inline polarization controller	500
Optical isolator:	**1358**
AC Photonics broadband fiber optic isolator IS83P22111	1358
Spectrometer:	**3300**
• ISG LW-SLIS-2048a-1394 high speed line camera	1800
• Wasatch 1800 lines/mm, 840 nm blaze HD volume phase grating, 38 mm square	750
• Nikon AF 85 mm f/1.8D	395
• Oz Optics HPUCO-23A-800/880-S-75AC-SP receptacle style collimator, 75 mm focal length	355
Sample and reference arms:	**675**
• Thorlabs PT1–1" translation stage	259
• 2-Oz Optics HPUCO-23A-830-S-10AC receptacle style collimator, 10 mm focal length	400
• Thorlabs ME05-M01-∅1/2″ round protected gold mirror, 3.2 mm thick	16
Miscellaneous mounting hardware:	**665**
Total	**8778**

out considering volume part discounts, this design is a fifth of the cost of comparable[20] biologically oriented SD-OCT systems while providing twice the FOV and similar acquisition rates (27 kHz versus 29 kHz), and sensitivity (97 dB estimated versus 91 dB).[20] In multiple (up to 100) unit production, bulk component discounts and direct buying could result in a further 15–20% cost reduction.

A complete system would also require custom interfacing with machining heads for specific applications. This can generally be accomplished by modifying a camera port and choosing the correct dichroic optic (not included in cost estimate due to high variability between applications) to combine the imaging and machining light. Additionally, an appropriate focused beam diameter for the imaging beam needs to be chosen. We expect that the imaging and machining light will be focused by the same objective (though this is not necessary) whose focal length is predetermined by existing machining process demands. Here, the choice of the sample arm collimator can be used to give the desired focal characteristics for imaging. Collimator alignment can also be used to compensate for focal length variation of the objective between imaging and machining light.

As an example application, we consider a machining laser head with a 100 mm focusing lens. To maintain uniform imaging over the depth of field, the collimator's focal length should be chosen so that the focused imaging beam's Rayleigh range is approximately half the system's depth of field. For the setup described above, we choose a 10 mm collimating lens and hence, expect a beam waist of 27 μm ($1/e^2$ intensity radius) and a Rayleigh range of 2.8 mm. Note that to achieve maximum axial resolution without additional computing load requires proper compensation of dispersion mismatch between the sample and reference arms.

The design is flexible and can be modified to improve the imaging rate (with an upgraded camera) or axial resolution. The latter is achieved by selecting a broader spectrum SLD and a grating with a reduced line density. This would provide significant resolution improvement with the drawback of reduced depth of field but little to no additional monetary cost. For instance, substituting the current components with an 840 ± 25 nm FWHM light source (Exalos EXS8410-F413) paired with a 1200 lines/mm grating (Edmund Optics NT48-589) could provide 6.2 μm resolution over a maximum range of 3 mm. Note that with higher spectral bandwidths, proper dispersion mismatch compensation is important to achieve maximum resolution.

In coherent imaging techniques such as this, if an interface moves by ~$\lambda/4$ or greater during the integration time of the detector, the fringe contrast will be significantly degraded ("washed out"), causing the signal from that interface to vanish.[21] This forms an upper limit to the interface speed that can be tracked. However, it also has the benefit of rejecting certain high speed interfaces (e.g., ejecta) that would produce reflections that complicate the images and make automatic feedback more difficult. The maximum interface speed depends on the integration time of the detector, which in turn affects sensitivity. For an integration time of 35 μs, the system can track interfaces moving at speeds up to 0.006 m/s. For faster moving interfaces, integration time can be reduced (at the expense of sensitivity) to 1 μs or 100 ns to give maximum speeds of 0.21 or 2.1 m/s, respectively. Since this is faster than typical etch rates in industrial processes, we expect that this design will be adequate for a wide range of applications.

IV. HOMODYNE DEPTH FILTERING

To use ICI as an automatic feedback method, processing must be able to run at least as fast as data acquisition. In biological imaging, the interpolation and FFT operations are necessary to calculate the reflected intensity from all the
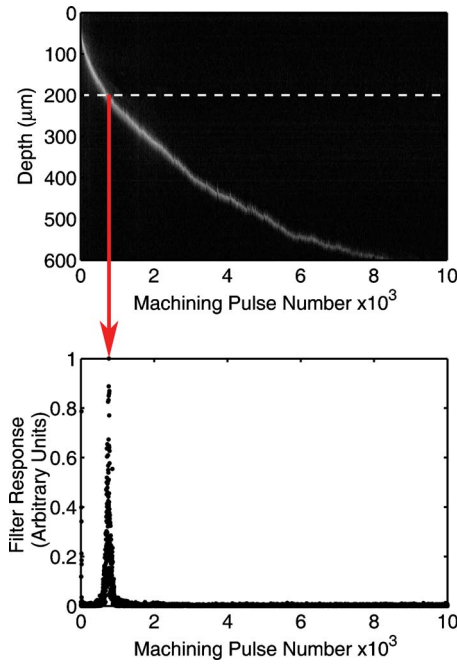
FIG. 3. The fully processed M-mode image from Fig. 1 with a white dashed line superimposed at the selected filter depth (top). The response from the homodyne filter exhibits a sharp peak as the machining front crosses the selected depth (bottom).

FIG. 4. A logic tree for simple feedback control using the homodyne filter algorithm.

depths within the FOV to form an image. By contrast, an anticipated role for feedback systems will be to trigger a change in the machining system (e.g., terminate emission) once a certain depth has been reached. In this case, calculating the reflectivity from all the depths is excessive. Instead, we demonstrate a simple and efficient software method for determining when drilling has penetrated a prescribed depth.

Starting with a desired depth, z, and using Eq. (1) with calibration data from the spectrometer, one can back-calculate a synthetic interferogram expressed in units of constant camera pixel number. This calculation can be completed *a priori* and does not contribute to the real-time computing load. By homodyne mixing the synthetic interferogram with the raw data from the camera, the signal from the desired depth can be extracted.

To demonstrate, we apply this filter technique to the spectrometer data used in Fig. 1, choosing a 200 μm target depth (indicated by a green line in Fig. 3). The filter response shows a clear and high signal-to-noise ratio response at the moment the machining front passes through the depth (Fig. 3 bottom). The fidelity of the data produced by homodyne filtering has been verified with the standard biological imaging code (background subtraction, cubic spline interpolation, FFT, and noise floor equalization) by comparing processed results from imaging data taken in a variety of situations including static interfaces, moving mirrors, percussion drilling, and biological samples.

The filter response can be used to trigger a feedback response to stop drilling. In Fig. 4, we present a scheme for software-based automatic feedback logic that controls drilling until a prescribed depth is reached. More complicated
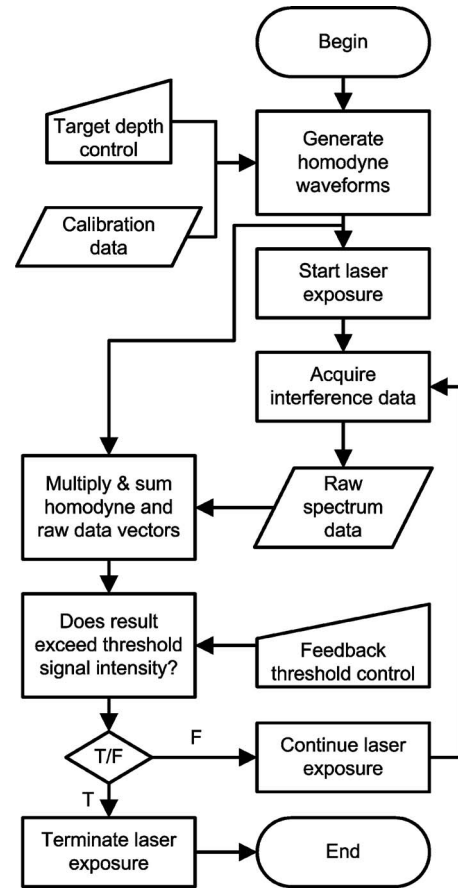
control systems with feedback from multiple depths and control of other parameters of the process are also possible. As each homodyne waveform can be calculated *a priori*, a look-up-table could be employed to rapidly and dynamically change the depth(s) of interest with no moving parts.

Depth filtering achieves considerable computational savings versus standard processing. We measured the time required to process multiple blocks of 576 element lines of previously acquired raw experimental data with both our standard biological imaging code and with the homodyne filter. Processing was conducted with a single thread running matlab on a quadcore Intel desktop CPU in a Microsoft Windows 7 64-bit environment. The results in Table III are ex-

TABLE III. Comparison of processing speed for 4×10^5 image lines.

Block size (A-lines)	Interpolation+FFT (IF) speed (klps)	Homodyne filter (HF) speed (klps)	Relative speed (HF/IF)
2×10^5	0.77	451.2	588
2×10^4	5.096	522.2	102
2×10^3	4.596	555.6	121
200	1.861	794.0	427
20	0.241	746.0	3097

pressed in terms of 10^3 lines per second (klps) and the relative speed increase factor obtained by using the homodyne filter.

For very small and very large block sizes, the FFT method is very slow. This is a result of limitations specific to the hardware and software environment and not the computational complexity of the code. As a result, the best theoretical comparison between the two methods is the midsize blocks. Here, even when the FFT produces its best results, the homodyne filter still outperforms it by two orders of magnitude. The primary reason for the difference in speed is that the homodyne filter avoids the interpolation step and calculates only the useful subset of the information that is obtained by the FFT.

While the line period limits the raw throughput rate, it is only a minimum value for the total feedback latency. Interrupt latency and other delays inherent to desktop hardware and operating systems are additive and may ultimately be the dominant terms. For this reason, we anticipate that the full capabilities of ICI-based feedback will not be realized without the use of dedicated processing hardware in the form of field programmable gate arrays (FPGAs) or application-specific integrated circuits. These components already exist in many modern cameras, including the one specified here. The ease of implementation of the homodyne filter algorithm described here onboard a camera would circumvent the desktop PC bottleneck and allow the camera itself to discipline the machining system.

V. CONCLUSION

ICI has the potential to provide real-time feedback control to industrial laser processes. However, the cost of equipment and computational overhead impedes widespread adoption. We have proposed a low cost ICI system that is suitable for integration into existing industrial processes. Additionally, we have proposed and tested an algorithm that is suitable for feedback control applications and increases processing rates by two orders of magnitude. The benefits and costs of the technology are anticipated to improve with the future use of dedicated hardware and FPGAs.

ACKNOWLEDGMENTS

[1] P. W. Leech, "Laser ablation of multilayered hot stamping foil," J. Mater. Process. Technol. **209**, 4281–4285 (2009).

[2] V. N. Tokarev, J. Lopez, and S. Lazare, "Modelling of high-aspect ratio microdrilling of polymers with UV laser ablation," Appl. Surf. Sci. **168**, 75–78 (2000).

[3] A. Kumar, M. Sapp, J. Vincelli, and M. C. Gupta, "A study on laser cleaning and pulsed gas tungsten arc welding of Ti-3Al-2.5V alloy tubes," J. Mater. Process. Technol. **210**, 64–71 (2010).

[4] M. M. A. Khan, L. Romoli, M. Fiaschi, F. Sarri, and G. Dini, "Experimental investigation on laser beam welding of martensitic stainless steels in a constrained overlap joint configuration," J. Mater. Process. Technol. **210**, 1340–1353 (2010).

[5] N. C. Nayak, Y. C. Lam, Y. C. Yue, and A. T. Sinha, "CO_2-laser micromachining of PMMA: the effect of polymer molecular weight," J. Micromech. Microeng. **18**, 095020 (2008).

[6] B. Pratap, C. B. Arnold, and A. Pique, "Depth and surface roughness control on laser micromachined polyimide for direct-write deposition," Proc. SPIE **4979**, 217 (2003).

[7] P. M. Lonardo, D. A. Lucca, and L. De Chiffre, "Emerging trends in surface metrology," CIRP Ann. **51**(2), 701–723 (2002).

[8] V. V. Temnov, K. Sokolowski-Tintenm, P. Zhou, and D. von der Linde, "Femtosecond time-resolved interferometric microscopy," Appl. Phys. A: Mater. Sci. Process. **78**, 483–489 (2004).

[9] J. Dietrich, M. Brajdic, K. Walther, A. Horn, L. Kelbassa, and R. Poprawe, "Investigation of increased drilling speed by online high-speed photography," Opt. Lasers Eng. **46**, 705–710 (2008).

[10] R. Lausten and P. Balling, "On-the-fly depth profiling during ablation with ultrashort laser pulses: A tool for accurate micromachining and laser surgery," Appl. Phys. Lett. **79**, 884–886 (2001).

[11] P. J. L. Webster, J. X. Z. Yu, B. Y. C. Leung, M. D. Anderson, V. X. D. Yang, and J. M. Fraser, "In situ 24 kHz coherent imaging of morphology change in laser percussion drilling," Opt. Lett. **35**, 646–648 (2010).

[12] A. F. Fercher, W. Drexler, C. K. Hitzenberger, and T. Lasser, "Optical coherence tomography − principles and applications," Rep. Prog. Phys. **66**, 239–303 (2003).

[13] P. J. L. Webster, J. X. Z. Yu, B. Y. C. Leung, M. D. Anderson, T. P. Hoult, and J. M. Fraser, "Coaxial real-time metrology and gas assisted laser micromachining: Process development, stochastic behavior and feedback control," Proc. SPIE **7590**, 759003 (2010).

[14] J. X. Z. Yu, P. J. L. Webster, B. Y. C. Leung, and J. M. Fraser, "High quality percussion drilling of silicon with a CW fiber laser beam," Proc. SPIE **7584**, 75840W (2010).

[15] P. J. L. Webster, M. S. Muller, and J. M. Fraser, "High speed in situ depth profiling of ultrafast micromachining," Opt. Express **15**, 14967–14972 (2007).

[16] P. J. L. Webster, B. Y. C. Leung, V. X. D. Yang, and J. M. Fraser, "Guidance of hard tissue ablation by forward viewing optical coherence tomography," Proc. SPIE **7554**, 75540Z (2010).

[17] M. W. Lindner, P. Andretzky, F. Kiesewetter, and G. Hausler, "Spectral Radar: Optical Coherence Tomography in the Fourier Domain," *Handbook of Optical Coherence Tomography*, edited by E. Bouma and G. J. Tearney (Marcel Dekker, New York, 2002), pp. 335–357.

[18] M. Wojtkowski, R. Leitgeb, A. Kowalczyk, T. Bajraszewski, and A. F. Fercher, "In vivo human retinal imaging by Fourier domain optical coherence tomography," J. Biomed. Opt. **7**, 457–463 (2002).

[19] R. Leitgeb, C. K. Hitzenberger, and A. F. Fercher, "Performance of fourier domain vs. time domain optical coherence tomography," Opt. Express **11**, 889–894 (2003).

[20] Thorlabs, Optical Coherence Tomography Imaging Systems, Thorlabs Product Catalogue V20, 2010, pp. 1353–1393.

[21] S. H. Yun, G. J. Tearney, J. F. de Boer, and B. E. Bouma, "Motion artifacts in optical coherence tomography with frequency-domain ranging," Opt. Express **12**, 2977–2998 (2004).